ACS APPLIED MATERIALS & INTERFACES

Research Article

www.acsami.org

Colored and Transparent Oxide Thin Films Prepared by Magnetron Sputtering: The Glass Blower Approach

Jorge Gil-Rostra,[†] Jesús Chaboy,[‡] Francisco Yubero,[†] Antoni Vilajoana,[§] and Agustín R. González-Elipe*[,†]

[†]Instituto de Ciencia de Materiales de Sevilla (CSIC-USE), Avda. Américo Vespucio 49, E-41092 Sevilla, Spain

[‡]Instituto de Ciencia de Materiales de Aragón (CSIC-UNIZAR), C/Pedro Cerbuna 12, E-50009 Zaragoza, Spain

[§]INDO Lens Group, C/Alcalde Barnils, 72. E-08174 Sant Cugat del Vallès, Barcelona, Spain

Supporting Information

ABSTRACT: This work describes the reactive magnetron sputtering processing at room temperature of several mixed oxide $M_xSi_yO_z$ thin films (M: Fe, Ni, Co, Mo, W, Cu) intended for optical, coloring, and aesthetic applications. Specific colors can be selected by adjusting the plasma gas composition and the Si−M ratio in the magnetron target. The microstructure and chemistry of the films are characterized by a large variety of techniques including X-ray photoemission spectroscopy, X-ray absorption spectroscopy (XAS), and infrared spectroscopy, while their optical properties are characterized by UV−vis transmission and reflection analysis. Particularly, XAS analysis of the M cations in the amorphous thin films has provided valuable information about their chemical state and local structure. It is concluded that the M cations are randomly distributed within the SiO_2 matrix and that both the M concentration and its chemical state are the key parameters to control the final color of the films.

KEYWORDS: *$M_xSi_yO_z$, reactive magnetron sputtering, colored thin films, optical properties*

INTRODUCTION

From the discovery of pottery to the development of glass, color has played a key role in the manufacturing of household and ornamental products.[1] Roman and mediaeval glasses were tinted to comply with the desire of the clients or for religious or artistic motivations as in the case of the stained glass windows of the gothic churches.[2] Probably one of the best hidden secrets in the realm of the glass blower artisans concerned the recipes used to furnish a specific color to the glass.[3] Today, the glass technology has made significant advances, and these old empirical recipes have evolved into well-established scientific procedures relying on the formation of solid solutions consisting of a transparent glass matrix and transition metal cations or metal nanoparticles embedded in their structure.[4,5] However, these principles, which are well-known to tint bulk glass, have been scarcely utilized in the field of thin film technology. Bright colored layers are for example made of metallic nitrides, oxynitrides, and related compounds.[6,7] Colored Bragg reflector mirrors made by stacking several layers of transparent materials with different refractive indices are also widely utilized for optical, ophthalmic, and related applications.[8−10] More recently the incorporation of silver or gold nanoparticles in thin film oxides has also been attempted, particularly in relation with the plasmon resonance effects of these metal nanoparticles and the biocide properties attributed to silver.[11−14] To our knowledge, the preparation of colored layers following a glass blower approach has not been systematically addressed in the field of thin film technology, except for a patent related with the ophthalmic lenses[15] and other scarce reports.[16]

Magnetron sputtering (MS) is a powerful technique of preparation of thin films which is widely utilized at both laboratory or industrial scales for the preparation of different kinds of single[17] or mixed[18,19] oxides or other complex oxide-based layers.[20−22] A typical example of high technological interest is the synthesis of transparent and conducting mixed oxides formed by the incorporation of two or more metal cations and where a complete transparency in the whole solar spectral range is a requisite.[18,19] In the field of solar collection applications, metal-oxide cermets films intended as selective absorbing coatings[20,21] or metal oxide layers with controlled amounts of nitrogen[22] used for visible light sensitization have also been prepared by this technique. The present work presents a description of MS preparation of colored, partially transparent oxide layers consisting of mixtures of a transparent oxide matrix and an absorbing transition metal cation, the latter being responsible for providing color to the films. This work is the continuation and generalization of the principles of a methodology previously outlined for $Cu_xSi_yO_z$ colored layers[23] and $W_xSi_yO_z$ films intended for electrochromic applications.[24]

Received: November 20, 2012
Accepted: February 22, 2013
Published: February 22, 2013

Besides presenting the principles of the method, we also describe how the concentration and chemical state of the transition metal cation, the film thickness, the bonding structure, and other factors affect the final color of the films. To this end we have performed a systematic study of the microstructure, chemical composition, local bonding structure, and optical properties of the films. The following types of thin films, each one intended for a specific coloration, have been prepared and characterized: $Cu_xSi_yO_z$ (green-brownish), $Fe_xSi_yO_z$ (yellowish-red), $Ni_xSi_yO_z$ (gray), $Mo_xSi_yO_z$ (pale blue), $W_xSi_yO_z$ (deep blue), and $Co_xSi_yO_z$ (orange-brownish). The careful characterization of the films by means of X-ray photoemission spectroscopy (XPS), X-ray absorption spectroscopy (XAS), and Fourier transform infrared spectroscopy (FT-IR) has served to get credited information about the chemical state and geometry around the metal cations. Particularly, the use of XPS and XAS, this latter in conjunction with sophisticated computational methods of spectral analysis, has resulted to be very valuable to this end and, in general, for the analysis of amorphous oxide thin films where structural and chemical information is quite elusive.

EXPERIMENTAL METHODS

Thin Film Preparation. $M_xSi_yO_z$ (M a transition metal cation) thin films have been prepared by reactive MS using a silicon target of 50 mm diameter on which a series of metal strips (Goodfellow 99.95%) have been arranged axially as reported in Figure S1 of the Supporting Information. The width of the strips was 1.5−2.0 mm. For each cation M, a series of samples were prepared with a different number of strips along the target diameter. As evidenced by the erosion track formed in the target (a circumference with ∼20 mm radius, i.e., 125 mm circumference length), the ratio between the Si and M sputtered areas varied depending on the number of metal strips wrapped around the Si target. Thin film growth was carried out at normal geometry with the substrates placed parallel to the magnetron. The distance between substrate and target was about 5 cm.

The magnetron was operated with a power of 100−300 W and a pulsed DC voltage of 250−500 V at a frequency of 80 kHz. The base pressure of the system was 3.0×10^{-6} mbar. The pressure during deposition was fixed at 5.0×10^{-3} mbar. The process gas consisted of O_2/Ar mixtures with mass flow ratios Φ_{O2}/Φ_{Ar} ranging from 0.05 to 2.5 depending on the type of thin film. The films were deposited on soda-lime glass and on Si(100) polished wafers. For direct assessment of color, they were also deposited on polymeric ophthalmic lenses and on commercial ceramic tiles. The samples will be named in the text with the following notation: $Mn - \Phi_{O2}/\Phi_{Ar}$, where M is the symbol of the cation, n is the number of metal strips wrapped around the target, and Φ_{O2}/Φ_{Ar} is the mass flow ratio between these two gases in the plasma discharge. Thus, for example, Fe3-0.1 corresponds to a thin film sample prepared with three iron strips wrapped around the Si target and $\Phi_{O2}/\Phi_{Ar} = 0.1$.

Thin Film Characterization. Elemental in-depth profiles and M/(M + Si) atomic ratios in the films were evaluated by Rutherford backscattering spectrometry (RBS). This characterization was performed in a 3 MeV tandem accelerator at the CNA (Sevilla, Spain) with a beam of 1.5−2.0 MeV alpha particles, about 2.0 nA beam current, accumulated doses about 1.5 μC, and ∼1 mm beam spot diameter. The RBS spectra were simulated with the SIMRNA software.[25]

FT-IR spectra were recorded in transmission mode in a Nicolet 510 spectrometer for samples deposited on polished undoped Si(100) wafers.

X-ray photoemission spectroscopy (XPS) was employed to assess the chemical state of the different elements present in the films at the surface of the samples. XPS spectra were recorded in a SPECS-PHOIBOS 100MCD spectrometer working in the constant pass energy mode at a value of 20 eV. The binding energy (BE) scale of the spectra was referenced to the C 1s peak of the spurious carbon contaminating the surface of the samples at a value of 284.5 eV. Fitting analysis of some of the photoelectron peaks after Shirley background subtraction was carried out with a series of doublet peaks with different binding energies to account for the oxidation and/or coordination states of the M^{n+} cations present in the samples.

X-ray absorption spectroscopy (XAS) experiments were carried out in the BM25 SPLINE beamline at the ESRF synchrotron in Grenoble (France). XAS spectra were recorded in the fluorescence mode at glancing configuration (80°), by using a 13-element Si(Li) detector (e2v Scientific Instruments). The energy of the incoming X-ray beam was tuned at the metal K-edge (L_3 in the case of W) with a Si(111) double-crystal monochromator, and harmonic rejection was achieved by detuning the second crystal from parallel alignment. X-ray absorption near edge spectroscopy (XANES) and extended X-ray Absorption Fine Structure (EXAFS) spectra were recorded at the K (Fe, Co, Ni, Cu, Mo) and L_3 (W) absorption edges of the corresponding elements in each series of samples.

The absorption spectra were analyzed according to standard procedures by using the ATHENA program which is included in the IFEFFIT program package that was also used to fit the theoretical EXAFS signals calculated by FEFF.[26] The computation of the XANES spectra was carried out with the multiple-scattering code CONTINUUM, included in the MXAN program pack,[27] based on the one-electron full-multiple-scattering theory. A complete discussion of the procedure can be found elsewhere.[28,29] The potential for the different atomic clusters was approximated by a set of spherically averaged muffin-tin (MT) potentials built by following the standard Mattheis prescription. The muffin-tin radii were determined following the Norman criterion. During the computations, special attention has been paid to determine the best choice for the overlapping factor between the muffin-tin spheres and for the exchange and correlation part of the final state potential.[30,31] It should be stressed that no free parameter has been used during the calculations. The theoretically calculated spectra have been directly compared to the experimental XANES spectra; i.e., no fitting procedure has been used. Besides, no free parameters have been employed in the calculations, so the quality of the theoretical computations is based on the correct reproduction of the shape and energy position of the different spectral features, their relative energy separation, and intensity ratio. In all the cases, the theoretical spectra have been convoluted with a Lorentzian shape function to account for the core-hole lifetime and the experimental resolution.[32] For the analysis of the Mo K and Ni K edges, we have followed the same computational procedure. First, we have determined the minimum size of the cluster needed to reproduce all the spectral features. This is made by adding progressively coordination shells surrounding the absorbing atom until convergence is obtained. In a second step, we have checked the influence of the overlapping factor among the muffin-tin spheres used to build up the scattering potential into the reproduction of the experimental XANES spectra. Initially, the computation of XANES has been made for a fixed size cluster by imposing a 10% overlapping factor, and then computations have been repeated by using lower, up to 1% (the default value in several codes), and higher, up to 20%, values. In addition we have also studied the effect of modifying the value of the maximum angular momentum quantum number, l_{max}, needed to account for the experimental absorption spectrum in the first ∼50 eV s. We have also checked the best choice of the exchange and correlation part of the final state potential (ECP) to reproduce not only the spectral shape but also the intensity of the computed spectral features and their relative energy separation. To this end we have performed the computations by using the energy-dependent Hedin−Lundqvist (HL) and Dirac−Hara (DH) ECP potentials. Moreover, we have also performed the computations by using only the real part of the HL ECP and by adding to the Dirac−Hara ECP the imaginary part of the HL one. The best reproduction of the experimental data has been obtained by using $l_{max} = 4$, an overlapping factor of 10%, and the real Dirac−Hara ECP potential. The use of complex potentials leads to an excessive damping of the main spectral features, while using the real HL potential leads to an unrealistic contraction of the energy scale, as

previously observed for different systems, including transition metal oxides.[31]

UV−vis transmission and reflection spectra were recorded in a Varian Cary 100 apparatus. From these curves, refractive index and extinction coefficient functions of the deposited films were derived by simulation of the measured spectra using the Forouhi−Bloomer formalism[33] for the description of the wavelength dispersion of the refractive index and extinction coefficient of the films.

The thin film microstructure (cross-sectional and planar views) of the films prepared on Si(100) was analyzed with scanning electron microscopy (SEM) using a Hitachi S4800 field emission electron microscope. For cross-sectional analysis thin film samples deposited on silicon were cleaved after dicing with a diamond tip.

RESULTS

1. Thin Film Microstructure and In-Depth Elemental Composition. The thin film microstructure was rather compact and homogeneous in all cases. As an example, Figure 1 shows the cross section (left) and planar view (right)

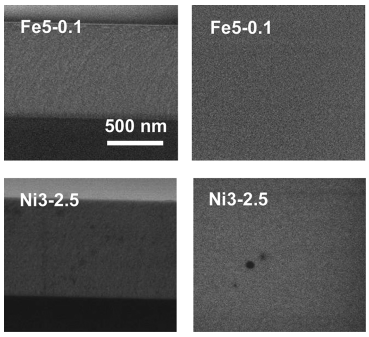

Figure 1. Cross section (left) and normal (right) micrographs of samples Fe5-0.1 (top) and Ni3-2.5 (bottom).

micrographs of samples Fe5-0.1 and Ni3-2.5. A similar compact and homogeneous microstructure was also depicted for all prepared films. This compact microstructure is related to the relatively short distance between the magnetron target and substrate during deposition. Typical thickness of the films investigated in this work was in the range of 300−800 nm.

The in-depth elemental composition of the films was checked by RBS. Figure 2 shows two selected examples corresponding to samples Fe3-0.1 and Fe5-0.1 showing in the two cases that the in-depth elemental distributions of iron and silicon atoms within the film are quite homogeneous. Similar flat profiles were obtained for the samples containing other cations and different atomic ratios M/(M + Si) (where M and Si are the atomic percentage of the metal M and silicon Si within the film). As a summary of the obtained results, Table 1 gathers the composition of the films containing the minimum and maximum M/(M + Si) ratios for each series of $M_xSi_yO_z$ samples. The other thin film compositions investigated in this work are between these two limits and are reported as Supporting Information (Table S2). We must note that RBS is not quite straightforward for quantitatively determining the oxygen content in thin films[34] and that therefore only information about the metals and silicon was retrieved from this analysis. The transparency and color of the films are directly appreciated in the two insets included in the figure.

2. Local Bonding Structure: FT-IR and XAS Analysis. To evaluate the origin of the color in the different $M_xSi_yO_z$ thin films it is important to assess whether the M^{n+} cations distribute as in a random solid solution within a SiO_2 matrix with the

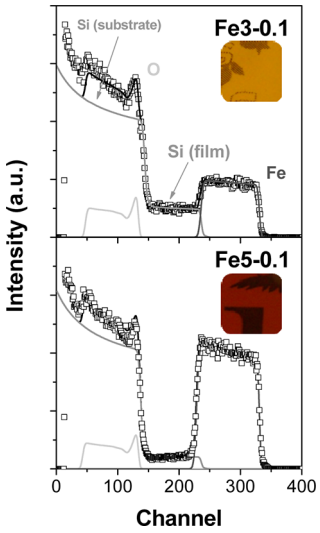

Figure 2. Experimental (hollow dots) and simulated RBS (full line) spectra of samples Fe3-0.1 (top) and Fe5-0.1 (bottom). Thin gray lines correspond to Fe, Si, and O elemental contributions to the simulated spectra. The inset images show views of the two samples deposited on soda-lime glass.

Table 1. M/(M + Si) Ratios, Refractive Indices, and Absorption Coefficients (at 550 nm) of Samples with the Minimum and Maximum Content of M for Each Series of Samples

series	sample	M/(M + Si)	n_{550}	k_{550}
$Cu_xSi_yO_z$	Cu1-1.0	0.24	1.54	0.001
	Cu5-1.0	0.67	2.11	0.142
$Ni_xSi_yO_z$	Ni1-1.0	0.07	1.49	0.002
	Ni3-0.1	0.61	1.71	0.029
$Fe_xSi_yO_z$	Fe3-1.0	0.30	1.61	0.008
	Fe5-0.1	0.73	2.31	0.073
$Co_xSi_yO_z$	Co1-0.1	0.20	1.52	0.013
	Co6-0.1	0.92	2.38	0.140
$Mo_xSi_yO_z$	Mo1-0.05	0.27	1.56	0.001
	Mo6-0.05	0.62	2.12	0.294
$W_xSi_yO_z$	W1-0.1	0.12	1.51	0.007
	W6-0.1	0.74	1.93	0.217

formation of Si−O−M bonding structures or if they agglomerate in segregated MO_x clusters with the preferential formation of M−O−M bonds. For the purpose of getting information about the local bonding arrangement around M, we have used the FT-IR and the XAS spectroscopies. The absence of peaks in the X-ray diffraction diagrams of the investigated samples confirmed their amorphous character.

In the past, we have used FT-IR spectroscopy to analyze the local bonding structure in mixed oxide thin films such as $Ti_xSi_yO_z$,[35] $Zr_xSi_yO_z$,[36] $Cu_xSi_yO_z$,[23] and $W_xSi_yO_z$[24] prepared at room temperature by ion, plasma, or magnetron sputtering techniques. A common result in these previous investigations was that, for low M/(M + Si) ratios, the cation M^{n+} was forming a solid solution within a silicon dioxide network where the relative amount of M−O−Si bonding structures was the majority. Moreover, as expected from pure probabilistic considerations, when the relative concentration of M increased, M−O−M bonding structures became the majority. A similar behavior has been found for the samples investigated in the present work. An example of the experimental evidence

dx.doi.org/10.1021/am302778h | ACS Appl. Mater. Interfaces 2013, 5, 1967−1976

sustaining this conclusion can be found in Figure 3 showing the FT-IR spectra of selected samples of $Ni_xSi_yO_z$ and $Mo_xSi_yO_z$

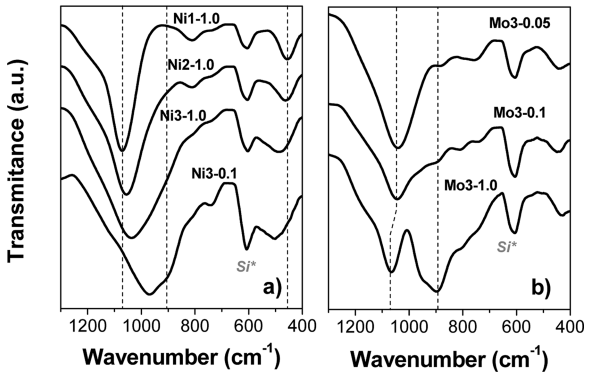

Figure 3. FT-IR spectra of $Ni_xSi_yO_z$ (a) and $Mo_xSi_yO_z$ (b) samples with different concentrations of M prepared with different Φ_{O2}/Φ_{Ar} ratios in the plasma gas. Vertical dashed lines highlight the typical vibrational bands attributed to Si−O−Si, M−O−Si, −M═O, and M−O−M(Si) bonding structures identified in the films (see text). A peak due to the silicon substrate is indicated.

thin films. In this figure, the band shape and intensity reveal a clear evolution from the spectrum of sample Ni1-1.0 to that of sample Ni3-1.0. In the former case, the main feature is a peak at around 1070 cm^{-1} which is recognized as the Si−O−Si stretching vibration of SiO_2.[37] This peak broadens and shifts to lower wavenumbers as the concentration of Ni in the film increases indicating a progressive formation of Ni−O−Si(Ni) bond structures (i.e., a random distribution of Ni and Si in an amorphous network). This evolution ends up with the formation of a broad shoulder centered at 905 cm^{-1} for the sample with the highest concentration of Ni (i.e., sample Ni3-0.1). The progressive displacement of this band toward lower wavelengths as the nickel concentration increases supports the preferential formation in this sample of Ni−O−Ni(Si) structures in agreement with a lower relative amount of silicon when lowering the Φ_{O2}/Φ_{Ar} ratio in the plasma discharge for sample Ni3-0.1. We attribute this effect to changes in the relative sputtering yield of silicon and nickel as a function of the oxygen content in the plasma gas, a parameter that does not affect the average oxidation state of nickel that was similar for samples Ni3-1 and Ni3-0.1 (see the XAS analysis in the Supporting Information, Figure S3). This evolution in band shape and position was common for the other $M_xSi_yO_z$ thin films where, similarly, the initial Si−O−Si and M−O−Si randomly distributed bonding structures evolves into M−O−M(Si) local arrangements as the concentration of M in the films increases.[38,39] The absence of any appreciable segregation in the form of MO_x clusters in the films with less concentration of M (e.g., no hint of any band or shoulder at around 900−1000 cm^{-1} can be seen in the spectrum of sample Ni1-1.0) agrees with the fact that deposition of highly energetic particles (few eV kinetic energy) and ion bombardment effects during the thin film growth[40] induce the mixing of the deposited atoms even at room temperature.

Besides this common trend in FT-IR bands reflecting the evolution from a M−O−Si to a M−O−M(Si) local structure, in the $W_xSi_yO_z$ and $Mo_xSi_yO_z$ thin films additional spectral features denoting the formation of O−M═O bonding structures were found for samples prepared under certain experimental conditions. For the $W_xSi_yO_z$ thin films the formation of such structures was discussed in a previous publication.[24] For the $Mo_xSi_yO_z$ thin films, the FT-IR spectra in Figure 3(b) corresponding to samples prepared with the same number of M strips show the formation of an intense and broad band at approximately 900 cm^{-1} when the Φ_{O2}/Φ_{Ar} ratio increases. In typical MoO_3 and polymolibdate compounds, a similar band has been attributed to the formation of Mo═O double bonds.[41] For the set of $Mo_xSi_yO_z$ samples reported in Figure 3(b), the appearance of this band occurs when an oxygen-rich plasma discharge is used for the MS deposition, indicating the development of such bonding structure for fully oxidized samples.

XAS analysis further sustains the previous assessment of the local structure around M while, simultaneously, provides additional information about the chemical state of the M^{n+} cations in the films. In general, the XAS analysis of metal cations in amorphous mixed oxide networks is not quite straightforward because of damping effects of the EXAFS amplitude and the broadening of the spectral features due to the spread of bonding distances around their mean values. Taking this restriction into account we have limited the present analysis to those spectra presenting well-defined shapes and where the methods of theoretical evaluation can be applied with less ambiguity. As examples to illustrate these possibilities we have selected series of $Co_xSi_yO_z$, $Mo_xSi_yO_z$, and $Ni_xSi_yO_z$ thin films, the data of these latter reported as Supporting Information (Figure S3).

In the case of the $Co_xSi_yO_z$ samples, chemical information was directly obtained from a simple fingerprint analysis of the XANES spectra. As shown in Figure 4, the Co K-edge

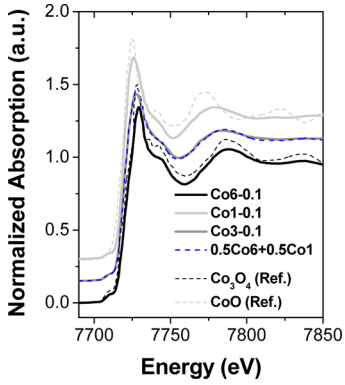

Figure 4. Co K edge experimental and simulated (blue dashed line superimposed on the Co3-0.1 spectrum) XANES spectra of the indicated $Co_xSi_yO_z$ samples and experimental spectra of CoO and Co_3O_4 references.

absorption spectrum of sample Co6-0.1 matches pretty well that of Co_3O_4, as evidenced by the similar position for the first oscillation after the absorption edge in the zone around 7775 eV. Meanwhile, the spectrum of sample Co1-0.1 resembles the one of CoO with a rather coincident position of this first oscillation. This proves that there is no trace of Co^{3+} species in this latter film. In the case of sample Co3-0.1 the situation is more complex, and the XANES spectrum could be reproduced as the weighted sum (50%) of the spectra of samples Co6-0.1 and Co1-0.1. Thus, the simultaneous presence of Co^{3+} and Co^{2+} species must be assumed for this sample. These results, obtained for samples prepared with the same gas plasma composition and different concentrations of Co, clearly indicate

that by increasing the amount of this element in the film the Co^{3+} oxidation state becomes progressively stabilized. We attribute this tendency to the expected formation of a local environment rich in Co as a second neighbor that would resemble the local arrangement in the Co_3O_4 spinel. In this line, previous works dealing with the deposition of cobalt oxide layers on SiO_2 substrates have shown that, under similar deposition conditions, the Co^{2+} state forms in the first layers directly interacting with the SiO_2 (i.e., the formation of Co−O−Si bonding structures would favor the stabilization of Co^{2+} species) and that Co^{3+} only starts to form for relatively thicker layers of the deposited oxide.[42]

The simple fingerprint and linear combination approach used with the $Co_xSi_yO_z$ samples could not be used for other $M_xSi_yO_z$ series of thin film samples, where first-principles calculations had to be applied to get credited information about the local environment around the M cations. The $Mo_xSi_yO_z$ samples constitute a first example where ab initio calculations are required to get structural information. The experimental Mo K-edge XANES and EXAFS spectra of the studied samples and of the reference compound $H_3Mo_{12}O_{40}P$ are shown in Figures 5

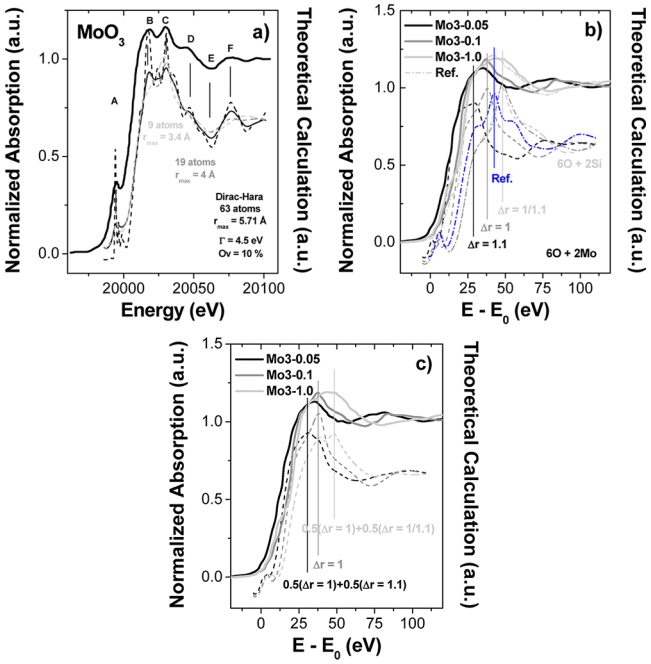

Figure 5. (a) and (b) Experimental (full lines) and theoretically calculated (dashed lines) Mo K edge XANES spectra of MoO_3, the indicated $Mo_xSi_yO_z$ samples, and experimental spectrum of the reference compound (dot-dashed line). (a) Ab initio simulation of the spectrum of MoO_3 by considering clusters of different sizes and number of atoms to reproduce the main features A−F of the experimental spectrum. (b) Reproduction of the experimental spectra of the indicated $Mo_xSi_yO_z$ amorphous samples and of the reference compound by considering a local arrangement consisting exclusively of 2Mo and 6O atoms separated by different atomic distances from the central Mo atom to reproduce the edge and maximum (indicated with vertical straight lines) positions in each case. A theoretical analysis of sample Mo3-1.0 by considering a local environmental formed by 6O and 2Si is also included (dot-dashed gray line). (c) Normalized experimental XANES spectra of the Mo K edge of $Mo_xSi_yO_z$ samples and their simulation by assuming for samples Mo3-0.05 and Mo3_1.0 a linear combination of theoretical spectra obtained with different interatomic distances as indicated.

and 6. The XANES spectra of the three studied $Mo_xSi_yO_z$ samples exhibit significant differences in both the spectral shape

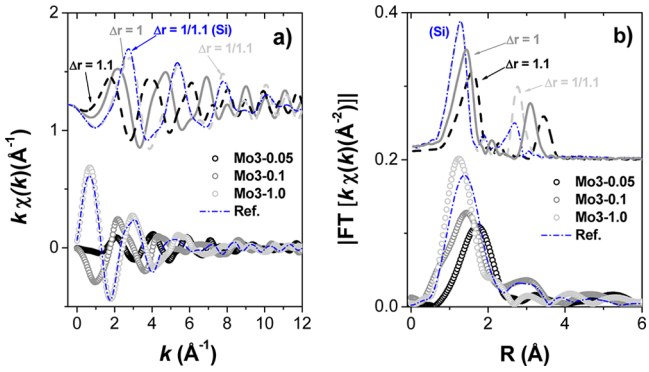

Figure 6. Experimental (bottom lines) and simulated (top lines) EXAFS (a) and FT (b) curves corresponding to the Mo K edge of the indicated $Mo_xSi_yO_z$ samples and the reference compound.

and the threshold position, both intimately linked to the local structure of the absorbing atom and the Mo−O interatomic distances.[29] The fact that the XANES spectrum of sample Mo3-0.05 shifts to lower energies indicates an increase of the interatomic distances with respect to those in sample Mo3-0.1, whereas the opposite effect is observed for sample Mo3-1.0. This is actually the tendency expected if, as suggested by the analysis of FT-IR spectra in Figure 3, Mo═O bonding structures become more abundant for the samples prepared with higher Φ_{O2}/Φ_{Ar} ratios. To verify these first structural assessments deduced from the XANES spectra we have performed ab initio computations as described in the Experimental Methods section. To this end we have tested the performance of the computations on the reference system MoO_3 where the absorbing Mo is surrounded by six oxygen atoms forming a distorted octahedron with interatomic distances ranging from 1.88 to 2.32 Å. As shown in Figure 5(a), the XANES spectrum of MoO_3 is well reproduced by using a cluster of 63 atoms, i.e., by including the scattering contributions of atoms located within the first 6 Å around the absorbing Mo. In addition, the same calculations performed on a cluster with only the first two coordination shells (6O + 2Mo) account well for the experimental XANES of sample Mo3-0.1. Then, we have studied the effect of modifying the interatomic distance on the edge-shift by increasing/decreasing the interatomic distances of this cluster by a factor of 1.1. As shown in Figure 5(b), the modification of the interatomic distances within this range reproduces the experimentally observed energy shift of the XANES spectra of samples Mo3-0.05 and Mo-1.0 with respect to that of Mo3-0.1. It should also be noted that the XANES spectrum of sample Mo3-1.0 is quite similar to that of the Mo^{6+} in the $H_3Mo_{12}O_{40}P$ reference compound. In this case, the shortest Mo−O distance is 1.68 Å, while it is 1.82 Å for Mo3-0.1, in agreement with the proposed modification of the interatomic distances. Finally, we have performed the same type of computations by substituting the Mo atoms in the second coordination shell by Si atoms. Despite the fact that this substitution does not introduce pronounced differences, especially at the zone region, the inclusion of Si in the second shell improves the agreement of the computed spectral shape at higher energies (Figure 5(b) and (c)). This result indicates that local Mo−O−Si environments are compatible with the experimental spectra of the

dx.doi.org/10.1021/am302778h | ACS Appl. Mater. Interfaces 2013, 5, 1967−1976

$Mo_xSi_yO_z$ samples that, to a first approximation, must be accounted for by a change in the average oxidation state (n) of Mo^{n+} according to n(Mo3-0.05) < n(Mo3-0.1) < n(Mo3-1.0). In this sense, the simulations have shown that the average interatomic distances decrease with the expected sizes of the Mo^{n+} cations and the formation of shorter Mo═O bonds in samples Mo3-1.0. It must be stressed that this tendency must not be considered a quantitative description of the local environment and oxidation states of Mo in the synthesized samples. A characteristic of these thin films is their structural complexity with large variations of local environments. This is clearly exemplified in Figure 5(b), showing that a reasonable good reproduction of the experimental spectral lines and not only of their edge and maximum positions can be obtained by a linear combination of two differently simulated spectra.

The previous results and tendencies were confirmed by using EXAFS, despite that the low signal-to-noise ratio of the EXAFS signals limited to 8 $Å^{-1}$ the range of analysis. In agreement with the Nyquist sampling theorem implying that only $2\Delta k\Delta r/\pi$ independent parameters can be determined from the data,[32] this fact prevents performing a standard EXAFS determination. Because of this reason we have restricted the analysis to a fingerprint computation of the EXAFS spectra by qualitatively comparing the experimental and theoretical signals calculated by using FEFF on the reference compound MoO_3. As shown in Figure 6 a good reproduction of the main spectral features and tendencies is obtained by assuming a change in the interatomic distances similar to that made to reproduce the XANES spectra. This analysis fully supports the conclusions derived from the analysis of the XANES region. Consequently, the combined XANES and EXAFS analysis provides useful information about both the short-range local order around Mo in the different samples as well as the modification of the Mo average oxidation state which is maximum Mo^{6+} for sample Mo3-1.0 and decreases progressively for Mo3-0.1 and Mo3-0.05 samples. Moreover, the theoretical simulations to reproduce the experimental spectra were in all cases similar and, for some spectral regions, even improved when Si substitutes Mo in the second coordination sphere, thus supporting the existence of Mo−O−Si bonding structures in the films, particularly in those with a low Mo/(Mo + Si) ratio where these bonding structures would be a majority.

Similar XAS analyses were carried out for the set of $Ni_xSi_yO_z$ samples where the equivalent oxidation state of nickel in all samples (i.e., Ni^{2+}) deduced from the shape of the spectra makes it easy to apply the methodology previously outlined for the $Mo_xS_yO_z$ thin films. A detailed analysis of the XANES and EXAFS spectra, reported as Supporting Information S3, sustains that in sample Ni1-0.1 nickel is diluted in a silicon oxide matrix with little or no nickel ions as second neighbors, while in sample Ni3-0.1, with a much higher content of nickel, this element has already a considerable number of other nickel atoms as second neighbors in a structure that resembles that of NiO.

3. Chemical States: XPS Analysis. From basic principles of coordination chemistry and colored glass manufacturing, it can be inferred that both the chemical state of the metal cation and its coordination state are critical factors in controlling the color of the films.[4,5] Besides the inference of chemical states of M made from the analysis of XANES spectra, more straightforward information about the oxidation state of the embedded cations can be obtained by XPS. Figure 7 shows a presentation with several spectra of the cations M present in

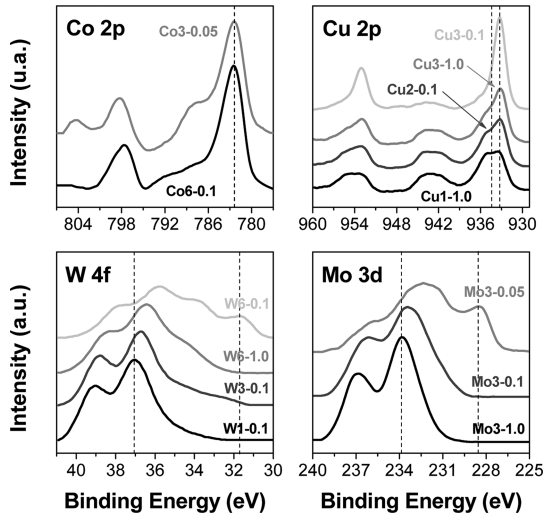

Figure 7. Co 2p, Cu 2p, W 4f, and Mo 3d XPS spectra of several $M_xSi_yO_z$ series of thin film samples as indicated.

different $M_xSi_yO_z$ thin film systems. Starting with the $Co_xSi_yO_z$ system, the shape of the Co 2p spectra clearly reveals an evolution from a Co^{2+} chemical state in sample Co3-0.05[42−44] to Co^{3+}[45,46] in sample Co6-0.1. This attribution agrees with literature data showing that spinel or Co^{3+}-containing systems are characterized by a Co2p doublet with no or very little intensity of the satellites at higher binding energies than the main peaks, while CoO or Co^{2+} containing systems depict a Co2p spectrum with a high intensity of these satellites.[42,45,46] This evolution in the oxidation state of cobalt agrees with the tendencies derived from the analysis of the XANES spectra in Figure 4, thus indicating that the cation oxidation state is similar at the surface and in the bulk of the films.

Chemical state changes for copper can also be deduced from the shape of the Cu 2p spectra in samples $Cu_xSi_yO_z$.[47] Thus, the spectral shape, particularly the low intensity of the satellite peak at the left of the main peak, is typical of Cu^+ species in samples Cu3-0.1. By contrast, the relatively high intensity of this satellite in sample Cu1-0.1 indicates that Cu^{2+} species are the majority here. Meanwhile, a mixture of Cu^+ and Cu^{2+} states can be deduced from the shape of the Cu 2p spectra in samples with an intermediate concentration of copper (e.g., in samples Cu2-1.0 and Cu3-1.0).

In samples $W_xSi_yO_z$ and $Mo_xSi_yO_z$, it appears that when the amount of Mo or W increases and/or the percentage of oxygen in the plasma gas decreases (i.e., from sample W1-0.1 to W6-0.1 and from sample Mo3-1.0 to Mo3-0.05) there is an increase in the intensity of the spectral region at the low binding energy side of the signal. The development of photoemission features in this spectral region is an indication of the formation of W^{n+} (n < 6) and Mo^{n+} (n < 6) states besides W^{6+} and Mo^{6+}.[24,48−50] The partition of the different oxidation states in each sample can be assessed by fitting analysis of the different spectra. An example of this analysis is reported in Figure 8 for the Mo 3d spectra showing that the experimental spectra are the sum of the contribution of Mo^{6+} (BE 233.8 and 232.5 eV), Mo^{5+} (BE 230.9 eV), and Mo^{4+}(BE 228.6 eV) chemical states.[49,50] Tentatively, we attribute the two Mo^{6+} components to molybdenum cations bonded to oxygen through either a single or a double bond. The relative concentrations of the different oxidation states of Mo in the series of $Mo_xSi_yO_z$ samples are gathered in Table 2. The inset images in this figure clearly

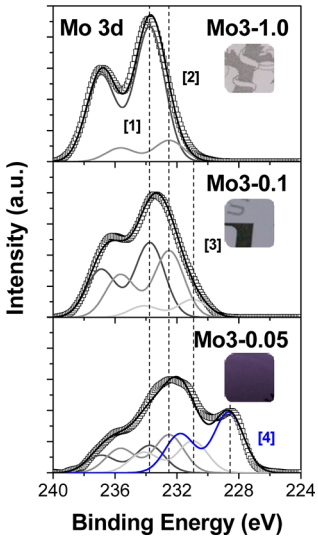

Figure 8. Fitted Mo 3d XPS spectra of selected $Mo_xSi_yO_z$ samples. Dashed vertical lines indicate the position of the different chemical states of Mo. The insert images illustrate the change of coloration produced by the formation of Mo^{n+} ($n < 6$) states in this series of samples deposited on soda-lime glass.

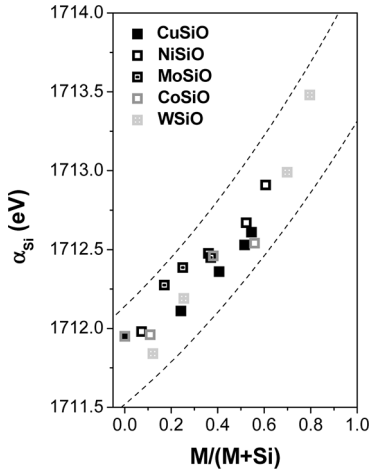

Figure 9. Evolution of the Auger parameter of Si with the M/(M + Si) ratio in the different series of $M_xSi_yO_z$ samples. Note that Si is present as Si^{4+} in all cases.

demonstrate that the development of color is linked with the formation of Mo^{n+} states ($n < 6$). A similar conclusion was previously deduced from the analysis of the $W_xSi_yO_z$ samples.[24]

Meanwhile, all the $Ni_xSi_yO_z$ samples were characterized by a similar Ni 2p spectral shape, typical of the Ni^{2+} state of this element.[51,52] This result indicates that irrespective of the deposition conditions nickel always appears as Ni^{2+} in these samples. Similarly, for all the $Fe_xSi_yO_z$ samples a Fe^{3+} oxidation state could be deduced from the analysis of the XPS spectra.

Another interesting change occurring when varying the M/(M + Si) ratio in the samples affects the Auger parameter of Si (α_{Si}).[35,53] This parameter is defined as the addition of the binding energy of the Si 2p peak and the kinetic energy of the Si $KL_{2,3}L_{2,3}$ Auger signal. Variations of this parameter for a fixed oxidation state are proportional to the differences in the extra-atomic relaxation energy of the photohole due to the changes in the local environment surrounding the atom (i.e., Si) undergoing photoemission.[54] A plot of α_{Si} as a function of the M/(M + Si) ratio for the different studied samples is shown in Figure 9. It is remarkable that all the points follow a common trend indicating that the relaxation energy of the photoholes[55,56] increases with the content of M in the films. This tendency agrees with the expected variation of the polarization energy of the different oxide matrices which, according to the Clausius−Mossotti relationship,[57] should increase with the polarizability of the constituent elements of the dielectric matrix. Additionally, the observed tendency sustains again that the films consist of a solid solution of the two cations in a common oxide network where the local polarizability should vary with the experimental M/(M + Si) ratio in each case.

The previous characterization results can be summarized with the conclusion that film composition and oxidation state of cations M are mainly determined by the number of strips in the target and by the plasma gas composition. The higher the number of strips in the target, the higher the concentration of M in the film. Similarly, the Φ_{O2}/Φ_{Ar} ratio in the plasma gas can also be used as an experimental parameter to control the oxidation state of the cations. In general, for oxides where the metal cation M may present different oxidation states (e.g., Cu, Mo, W), augmenting Φ_{O2}/Φ_{Ar} favors the formation of their most oxidized forms. An exception is cobalt where the ratio Co/Si favors the stabilization of Co^{3+} species in the films. By contrast, silicon always appears as Si^{4+}, in agreement with the high tendency of this element to become oxidize. The sputtering process from the metallic targets is mainly the result of the impingement of the Ar^+ ions, while reactions of the sputtered atoms with molecular or excited oxygen species present in the plasma, either during their fly to the substrate or once they have arrived to the surface of the growing film, produce the oxidation of both elements, silicon and the cation M.

4. Optical Properties of the $M_xSi_yO_z$ Thin Films. The optical properties of the films were drastically affected by the amount and oxidation state of the cation M in the films. Examples of this influence are shown in the form of images in Figure 10 for the $Ni_xSi_yO_z$ samples. A quantitative evaluation of the change in the optical properties can be made by using the UV−vis spectroscopy. Figure 10 also shows the transmission spectra of the investigated $Ni_xSi_yO_z$ films, as well as the derived refractive index $n(\lambda)$ and extinction coefficient $k(\lambda)$ curves. The transmission spectra, characterized by a broad absorption band

Table 2. Evolution of Oxidation States of the Cations in Some Selected $Mo_xSi_yO_z$ Samples with the Φ_{O2}/Φ_{Ar} Ratio in the Plasma Discharge

	[1]O=Mo^{6+}−O	[2]O−Mo^{6+}−O	[3]Mo^{5+}−O−	[4]Mo^{4+}−O−
BE (eV)	233.8	232.5	230.9	228.6
Mo3-1.0	0.86	0.14	-	-
Mo3-0.1	0.47	0.42	0.11	-
Mo3-0.05	0.17	0.24	0.20	0.39

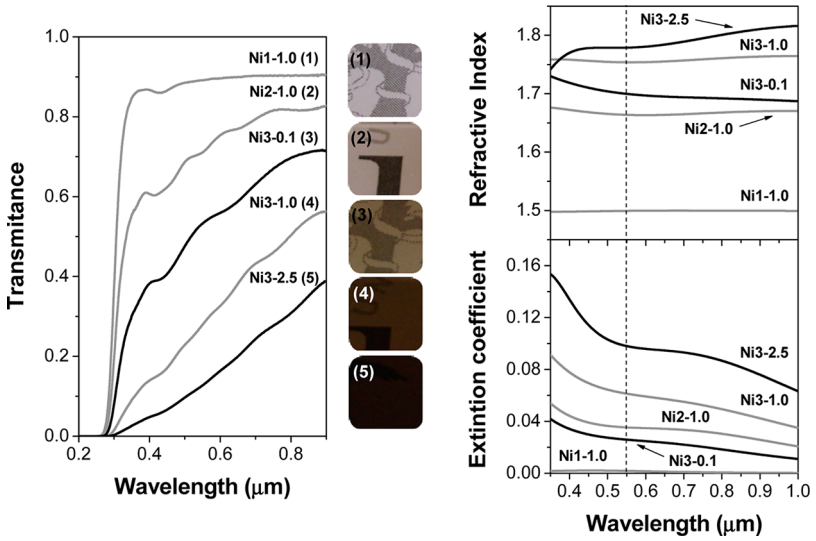

Figure 10. Optical properties of $Ni_xSi_yO_z$ thin films. (Left) UV−vis transmission spectra and images of the indicated films deposited on soda-lime glass. (Right) Refractive index and extinction coefficient derived from the reflectance spectra.

extending through the whole visible range, clearly indicate that film absorption increases with the amount of Ni and with the Φ_{O2}/Φ_{Ar} ratio. Meanwhile, the reflectance spectra (see Figure S4 in the Supporting Information) are characterized by a series of oscillations whose intensity increases as the content of oxygen in the plasma decreases. From these data it is possible to determine the extinction coefficient and refractive index of the studied films. The evolution for the series of curves reported in Figure 10 indicates that both $n(\lambda)$ and $k(\lambda)$ increase with the content of Ni in the films (i.e., number of strips during the preparation of the films) and, for the maximum number of strips, with the Φ_{O2}/Φ_{Ar} ratio. This latter effect must be related with a certain deviation of stoichiometry, a result that in pure NiO is known to produce a darkening of the samples by the formation of a $NiO_{(1+x)}$ state.[58] We must note that this slight deviation is compatible with the determination by XPS and XAS that the oxidation state of nickel is Ni^{2+} and only indicates a slight increment in the number of holes in the amorphous lattice.

The optical properties of the other $M_xSi_yO_z$ films followed different variations depending on the amount of metal and its average oxidation state. As a summary, Figure 11 shows the extinction coefficient curves obtained for selected $M_xSi_yO_z$ thin films (M: Fe, Ni, Co, Cu, Mo, W) prepared with a different number of metal strips in the cathode and Φ_{O2}/Φ_{Ar} ratios in the plasma gas. The different shapes of these curves and the images included in the same figure clearly support that it is possible to produce a great variety of colors in $M_xSi_yO_z$ films prepared by magnetron sputtering at room temperature by just varying the nature of M and other experimental conditions during deposition.

To further illustrate the versatility and possibilities of the procedure, Figure 12 shows a series of ophthalmic lenses and ceramic plates covered with $M_xSi_yO_z$ thin films depicting different colors. It is apparent from this figure that either transparent or white substrates can be differently tinted by using the developed procedure. For a better evaluation of the colors obtained for each set of samples, the color diagram included in Figure 12 represents the color coordinate regions covered by each one of the investigated thin film systems. Each region encompasses a large set of $M_xSi_yO_z$ thin films where

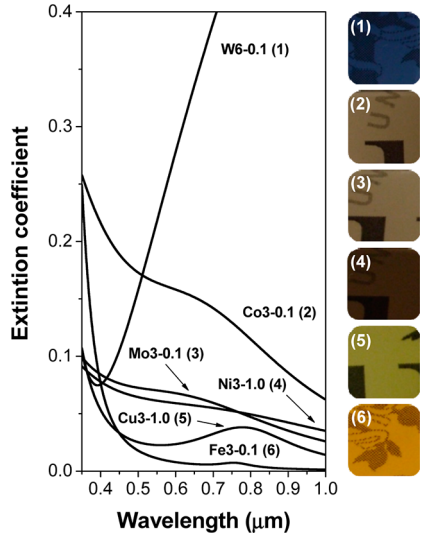

Figure 11. Extinction coefficient curves and pictures of the films deposited on soda-lime glass of selected $M_xSi_yO_z$ samples: (1) W6-0.1, (2) Co3-0.1, (3) Mo3-0.1, (4) Ni3-1, (5) Cu3-1, and (6) Fe3-0.1.

both the M/Si ratio and the oxidation state of the cations are systematically varied as explained in the previous sections. The visual effects are a consequence of the location in this color map of the particular coordinates of a given film. Thus, blue colors in $Mo_xSi_yO_z$ and $W_xSi_yO_z$ films can be associated with the formation of low oxidation states of Mo or W; green-brownish colors in $Cu_xSi_yO_z$ stem from the presence in a different concentration of Cu^+ and Cu^{2+} ions; gray-dark colors in $Ni_xSi_yO_z$ depend on the concentration of nickel and slight deviations in stoichiometry; yellow-orange colors in $Fe_xSi_yO_z$ are a result of the different concentration of iron in the films; while the brownish-orange aspect in the $Co_xSi_yO_z$ originates from the different concentration of cobalt responsible for stabilizing the Co^{2+} or Co^{3+} states of this element.

SUMMARY AND CONCLUSIONS

The results presented in this work have shown that it is possible to produce a large variety of semitransparent colored $M_xSi_yO_z$

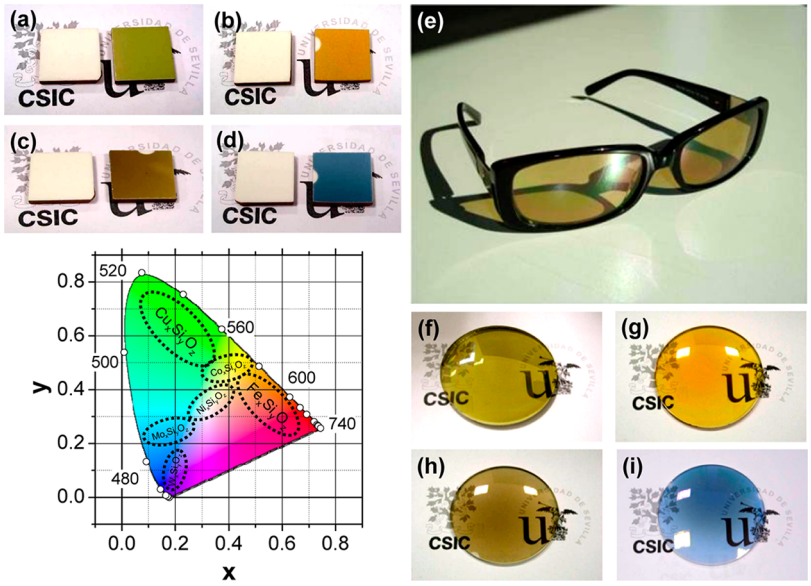

Figure 12. (Top) White ceramic plates (also in its pristine white form) and polymeric ophthalmic lenses (right), covered with different colored mixed oxide thin films: (a,f) $Cu_xSi_yO_z$, (b,g) $Fe_xSi_yO_z$, (c,h) $Co_xSi_yO_z$, (d,i) $W_xSi_yO_z$, (e) commercial sunglasses (Indo Lens Group) with ophthalmic lenses covered with $Cu_xSi_yO_z$. (Left-down) Color coordinate diagram with indication of the coordinate region covered by each series of thin film samples.

thin films by reactive magnetron sputtering deposition from a single cathode varying the relative M/Si ratio in the track etching zone of the cathode. For the sake of simplicity, in this exploratory work we modify this parameter by wrapping a variable number of strips of the metal M around a silicon cathode. The present investigation has determined the relationships between the film characteristics and the target compositions. Obviously, the use of mixed targets of known composition or carrying out a cosputtering from two targets would be more straightforward solutions at an industrial scale. Other virtues of the method to be highlighted are its easy up-scaling (as claimed in patent of ref 15), the possibility of using either a single alloyed target or two targets for sputtering, and its compatibility with any kind of substrate including glass, metals, ceramic, polymers, or other sensitive materials. The development of electrochromic and antireflective films or the possibility of controlling both the extinction coefficient and the refractive index of the film are additional advantages of the method. In the present work, this latter parameter is relatively low because of the use of SiO_2 as a matrix. Other alternatives (e.g., TiO_2, ZrO_2, etc.) would lead to thin films with higher refractive index and other possibilities of fine-tuning the color and other optical properties of the films. In all cases, the inorganic character of the films described in this paper makes them more stable against UV radiation than conventional colored films based on organic dyes much more sensitive to the light.

The characterization results of the present study have shown that it is possible to get films with variable compositions and, what is the most important in relation with the objectives of the work, a large variety of colors and optical properties. A difficulty associated with the characterization analysis of the films is related with their amorphous character which has endowed the development of relatively sophisticated analysis procedures, particularly in the case of the XAS and XPS spectroscopies.

In the visible, the films do not present any significant glare or mirrored reflection but a specific absorption that can be tuned by changing the nature of the metal cation, its relative concentration in the film, and its chemical state and local coordination arrangement, basically the same parameters that the ancient time and middle age artisans varied empirically to control the glass color. In comparison with the stain glasses, our films present in general a fainter coloration (i.e., less absorption intensity), although this difference has to do with the quite different thickness considered in each case, some hundreds of nanometers in our case and one or more millimeters in the case of glass. Thus, after several centuries and the contribution of a large variety of quite modern and powerful processing and characterization techniques, we have been able to get results in the line of those of the glass blowers but in the form of thin films and in a way that is compatible with an industrial process. However, we believe that, despite the progresses offered by the new technologies, the poetry, beauty, and mystery of the old stained glass windows will remain forever.

■ ASSOCIATED CONTENT

Supporting Information

Si−M mixed target configuration (Figure S1); M/(M + Si) ratios, refractive index and absorption coefficient (at 550 nm) for the series of mixed oxides thin films investigated in this work (Table S2); analysis of the XAS spectra of samples $Ni_xSi_yO_x$ (Figure S7 and associated brief discussion); experimental and simulated reflectance spectra of $Ni_xSi_yO_z$ thin films prepared on polished Si(100) (Figure S4). This material is available free of charge via the Internet at http://pubs.acs.org.

■ AUTHOR INFORMATION

Corresponding Author

*E-mail: arge@icmse.csic.es.

Notes

The authors declare no competing financial interest.

■ ACKNOWLEDGMENTS

We thank the Junta de Andalucía (Projects P09-CTS-5189, TEP5283, and FQM-6900), the Ministry of Science and Innovation (Projects CENIT-ArtDeco, CONSOLIDER CSD2008-00023, MAT2010-21228, MAT2010-18447, MAT2008-06542-C04-01, MAT2011-27573-C04-04), and DGA NETOSHIMA grants for financial support. We acknowledge MICINN and CSIC for provision of synchrotron radiation facilities at the ESRF and the BM25-Spline staff for the technical support. We also acknowledge the CNA for the RBS measurements.

■ REFERENCES

(1) Brown, S. *Stained Glass, an Illustrated History*, 2nd ed.; Brachen Books: London, 1995.
(2) Morris, E. *Stained and Decorative Glass*; Grange Books Ltd.: U.K., 1995.
(3) Theophilus; Hawthorne, J. G.; Smith, C. S. *On Divers Arts*; Dover Publications: Mineola, NY, 1979.
(4) Bach, H.; Neuroth, N. *The Properties of Optical Glass*, 2nd ed.; Springer: New York, 1995.
(5) Fernandez-Navarro, J. M. *El Vidrio*, 2nd ed.; CSIC: Madrid, 1991.
(6) Niyomsoan, S.; Grant, W.; Olson, D. L.; Mishra, B. *Thin Solid Films* **2002**, *415*, 187−194.
(7) Zhu, D.; Zhao, S. *Sol. Energy Mater. Sol. Cells* **2010**, *94*, 1630−1635.
(8) Boudaden, J.; Oelhafen, P.; Schüler, A.; Roecker, C.; Scartezzini, J. L. *Sol. Energy Mater. Sol. Cells* **2005**, *89*, 209−218.
(9) Wu, Z.; Lee, D.; Rubner, M. F.; Cohen, R. E. *Small* **2007**, *3*, 1445−1451.
(10) Eiamchai, P.; Horprathum, M.; Patthanasettakul, V.; Limnonthakul, P.; Nuntawong, N.; Limsuwan, P.; Chindaudom, P. *Mater. Des.* **2010**, *31*, 3151−3158.
(11) Torrell, M.; Machado, P.; Cunha, L.; Figueiredo, N. M.; Oliveira, J. C.; Louro, C.; Vaz, F. *Surf. Coat. Technol.* **2010**, *204*, 1569−1575.
(12) Ung, T.; Liz-Marzan, L. M.; Mulvaney, P. *J. Phys. Chem. B* **2001**, *105*, 3441−3452.
(13) Sangpour, P.; Akhavan, O.; Moshfegh, A. Z. *J. Alloys Compd.* **2009**, *486*, 22−28.
(14) Saulou, C.; Despax, B.; Raynaud, P.; Zanna, S.; Marcus, P.; Mercier-Bonin, M. *Appl. Surf. Sci.* **2009**, *256*, S35−S39.
(15) Fernandez-Serrano, R.; Vilajoana-Mas, A.; Dürsteler-López, J. C.; Gil-Rostra, J.; Yubero-Valencia, F.; González-Elipe, A. R. Polymer lens comprising a hardening layer, and absorbent layer, and a interferential multilayer and corresponding method, patent WO/2010/106200.
(16) Łączka, M.; Cholewa, K. *J. Alloys Compd.* **1995**, *218*, 77−85.
(17) Sato, H.; Minami, T.; Takata, S.; Yamada, T. *Thin Solid Films* **1993**, *236*, 27−31.
(18) Chopra, K. L.; Major, S.; Pandya, D. K. *Thin Solid Films* **1983**, *102*, 1−46.
(19) Minami, T. *Semicond. Sci. Technol.* **2005**, *20*, 35−44.
(20) Karmhag, R.; Tesfamichael, T.; Wackelgard, E. *Sol. Energy* **2000**, *68*, 329−333.
(21) Juang, R. C.; Yeh, Y.; Chang, B. H.; Chen, W. C.; Chung, T. W. *Thin Solid Films* **2010**, *518*, 5501−5504.
(22) Lindgren, T.; Mwabora, J. M.; Avendano, E.; Jonsson, J.; Hoel, A.; Granqvist, C. G.; Sten-Eric Lindquist, S. E. *J. Phys. Chem. B* **2003**, *107*, 5709−5716.
(23) Gil-Rostra, J.; Yubero, F.; Fernández, R.; Vilajoana, T.; Artús, P.; Dürsteler, J. C.; Cotrino, J.; Ortega, I.; González-Elipe, A. R. *Opt. Mater. Express* **2011**, *1*, 1100−1112.
(24) Gil-Rostra, J.; Cano, M.; Pedrosa, J. M.; Ferrer, F. J.; García-García, F.; Yubero, F.; González-Elipe, A. R. *ACS Appl. Mater. Interfaces* **2012**, *4*, 628−638.
(25) http://max-planck-institut-fuer-plasmaphysik.software.informer.com/, 2012.
(26) Ravel, B.; Newville, M. J. *Synchroton Radiat.* **2005**, *12*, 537−541.
(27) Benfatto, M.; Della Longa, S. J. *Synchrotron Radiat.* **2001**, *8*, 1087−1094.
(28) Chaboy, J.; Quartieri, S. *Phys. Rev. B* **1995**, *52*, 6349−6357.
(29) Chaboy, J. *Synchrotron Radiat.* **2009**, *16*, 533−544.
(30) Chaboy, J.; Maruyama, H.; Kawamura, N. *J. Phys.: Condens. Matter* **2007**, *19*, 216214−216222.
(31) Guglieri, C.; Chaboy, J. *J. Phys. Chem. C* **2010**, *114*, 19629−19634.
(32) Krause, M. O.; Oliver, J. H. *J. Phys. Chem. Ref. Data* **1979**, *8*, 329.
(33) Forohui, A. R.; Bloomer, I. *Phys. Rev. B* **1986**, *34*, 7018−7026.
(34) Xie, T.; Ryan, S. R.; Fischbeck, H. J. *Nuclear Instr. Methods Phys. Res., Sect. B* **1998**, *40*−*41*, 766−768.
(35) Gracia, F.; Yubero, F.; Holgado, J. P.; Espinós, J. P.; González-Elipe, A. R.; Girardeau, T. *Thin Solid Films* **2006**, *500*, 19−26.
(36) Ferrer, F. J.; Frutos, F.; García-López, F. J.; González-Elipe, A. R; Yubero, F. *Thin Solid Films* **2007**, *516*, 481−485.
(37) Han, S. M.; Aydil, E. S. *Appl. Phys. Lett.* **1997**, *70*, 3269−3271.
(38) Puskas, I.; Fleisch, T. H.; Full, P. R.; Kaduk, J. A.; Marshall, C. L.; Meyers, B. L. *Appl. Catal. A: Gen.* **2006**, *311*, 146−154.
(39) Miao, Y.; Lu, G.; Liu, X.; Guo, Y.; Wang, Y.; Guo, Y. *J. Ind. Eng. Chem* **2010**, *16*, 45−50.
(40) Welzel, T.; Naumov, S.; Ellmer, K. *J. Appl. Phys.* **2011**, *109*, 073302−073312.
(41) Zakharova, G. S.; Tischner, C.; Volkov, V. L.; Hellmann, I.; Klingeler, R.; Leonhardt, A.; Biichner, B. *Solid State Sci.* **2007**, *9*, 1028−1032.
(42) Jiménez, V. M.; Espinós, J. P.; González-Elipe, A. R. *Surf. Interface Anal.* **1998**, *26*, 62−71.
(43) Stern, E. A. *Phys. Rev. B* **1993**, *48*, 9825−9827.
(44) Corrias, A.; Mountjoy, G.; Piccaluga, G.; Solinas, S. *J. Phys. Chem. B* **1999**, *103*, 10081−10086.
(45) Jiménez, V. M.; Fernández, A.; Espinós, J. P.; González-Elipe, A. R. J. *Electron Spectrosc. Relat. Phenom.* **1995**, *71*, 61−71.
(46) Soriano, L.; Abbate, M.; Fernández, A.; González-Elipe, A. R.; Sirotti, F.; Sanz, J. M. *J. Phys. Chem. B* **1999**, *103*, 6676−6679.
(47) Espinós, J. P.; Morales, J.; Barranco, A.; Caballero, A.; Holgado, J. P.; González-Elipe, A. R. *J. Phys. Chem. B* **2002**, *106*, 6921−6929.
(48) Leftheriotis, G.; Papaefthimiou, S.; Yianoulis, P.; Siokou, A. *Thin Solid Films* **2001**, *384*, 298−306.
(49) Sian, T. S.; Reddy, G. B. *Sol. Energy Mater. Sol. Cells* **2004**, *82*, 375−386.
(50) López-Carreño, D. L.; Benítez, G.; Viscido, L.; Heras, J. M.; Yubero, F.; Espinós, J. P.; González-Elipe, A. R. *Surf. Sci.* **1998**, *402*−*404*, 174−177.
(51) González-Elipe, A. R.; Holgado, J. P.; Alvarez, R.; Munuera, G. *J. Phys. Chem.* **1992**, *96*, 3080−3086.
(52) Liu, H.; Zheng, W.; Yan, X.; Feng, B. *J. Alloys Compd.* **2008**, *462*, 356−361.
(53) Reiche, R.; Yubero, F.; Espinós, J. P.; González-Elipe, A. R. *Surf. Sci.* **2000**, *457*, 199−210.
(54) Wagner, C. D. *Faraday Discuss. Chem. Soc.* **1975**, *60*, 291−300.
(55) Moretti, G. *J. Electron Spectrosc. Relat. Phenom.* **1998**, *95*, 95−144.
(56) V.M. Jiménez, V. M.; A. Fernández, A.; J.P. Espinós, J. P.; A.R. González-Elipe, A. R. *Surf. Sci.* **1996**, *350*, 113−126.
(57) Ozerov, R. P.; Vorobyev, A. A. *Phys. Chem. Elsevier B.V.* **2007**, 251−304.
(58) Mihelčiča, M.; Jermana, F.; Šveglb, I.; Šurca-Vuka, A.; Slemenik-Peršea, L.; Kovačc, J.; Orela, B.; Possetd, U. *Sol. Energy Mater. Sol. Cells* **2012**, *107*, 175−187.